Stability of thiol-based self-assembled monolayer functionalized electrodes in EG-OFET-based applications

Tewari, Amit; Björkström, Kim; Ghafari, Amir Mohammad; Macchia, Eleonora; Torsi, Luisa; Österbacka, Ronald

Contents lists available at ScienceDirect

FlatChem

journal homepage: www.sciencedirect.com/journal/flatchem

Stability of thiol-based self-assembled monolayer functionalized electrodes in EG-OFET-based applications

Amit Tewari [a,b], Kim Björkström [a], Amir Mohammad Ghafari [a], Eleonora Macchia [a,c], Luisa Torsi [d], Ronald Österbacka [a,*]

[a] *Physics and Center for Functional Materials, Faculty of Science and Engineering, Åbo Akademi University, Turku 20500, Finland*
[b] *Faculty of Information Technology and Communication Sciences, Tampere University, Tampere 33720, Finland*
[c] *Dipartimento di Farmacia-Scienze del Farmaco, Università degli Studi di Bari Aldo Moro, Bari 70125, Italy*
[d] *Dipartimento di Chimica and Centre for Colloid and Surface Science, Università degli Studi di Bari Aldo Moro, Bari 70125, Italy*

ARTICLE INFO

ABSTRACT

The surface passivation of thermally deposited Au using n-alkanethiol self-assembled monolayers (SAMs) as insulating monolayers in electrolyte-gated organic-field effect transistor (EG-OFET) and its impact on EG-OFET operation has been clarified. We used three different n-alkanethiols derivates, namely propanethiol (P-SAM), hexanethiol (H-SAM), and octanethiol (O-SAM), with different chain lengths (C_3, C_6, and C_8). The non-uniform distribution of the used SAMs on the inhomogeneous Au surface significantly affects the net capacitance, i.e., the serial capacitance of the double layer (C_{DL}) and blocking layer (C_{BL}) capacitance of the functionalized gate. The SAM-functionalized gates were exposed to cyclic electrical stress (forward and reverse) for 128 cycles with gate voltage (V_G) sweep from 0.1 to -0.4 V at constant drain voltage ($V_D = -0.4$ V) and compared to a bulk-gold reference gate electrode. The registered transfer curves showed increased drain currents that saturated during prolonged cycling. Two figures of merit, i.e., threshold voltage (V_{th}) and hysteresis, were extracted from the recorded transfer curves, and their responses were studied separately. We found that both V_{th} and hysteresis increase with cycling. The change is small but constantly increases for the short-chain P-SAM, while for the longer-chain H- and O-SAM, the initial change is more prominent, reaching saturation after approximately 25 cycles. We have investigated the surface roughness of different gate electrodes through Atomic Force Microscopy (AFM) to confirm the packing density of thiol molecules. We also performed 80 h long-term stability data using cyclic voltammetry measurements for each thiol-functionalized electrode. No signs of desorption could be found, as evidenced by XPS. The results are consistent with previously suggested models for electrical transport across such SAMs, confirming that these monolayers restrict faradic processes at the electrodes by passivating the Au surface.

1. Introduction

Recent advancements in electrolyte-gated organic field-effect transistor (EG-OFET) based biosensors show great potential for future point-of-care diagnostic devices [1,2]. However, there are two main challenges frequently encountered during the sensing process. The first deals with minimizing unwanted faradaic currents that can cause device degradation, and the second is associated with achieving stable device operation [2,3]. Typically, a cleaned Au-electrode (either in bulk or in its thermally deposited form) is employed as a reference gate electrode to stabilize the device before and monitor the channel for degradation during sensing measurements. Polarizable electrodes, such as gold, tend to adsorb organic materials available in the measurement surroundings resulting in altered interfacial properties with drift or an incorrect detector response as an option [4]. One way of attaining a highly stable Au gate electrode would be by applying a passivating monolayer over the surface of the gate electrode.

Self-assembled monolayers (SAMs) based on n-alkanethiols have been extensively employed as surface passivating layers on metal surfaces [5–10]. These thiols form well-ordered, closed-packed, and uniform monolayers and act as molecular (charge) blocking layers [11]. Alkanethiol SAMs have been implemented to control the surface's
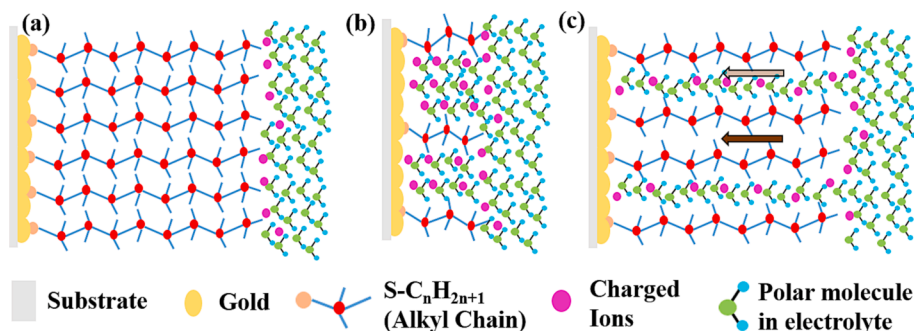
---

* Corresponding author.
E-mail address: ronald.osterbacka@abo.fi (R. Österbacka).

Fig. 1. Schematic illustration of (a) an ideally uniform alkanethiol monolayer film on smooth gold surfaces. (b) An inhomogeneous short-chain (P-SAM) monolayer distribution leads to pinholes and ion accumulation at the bare Au spots. (c) Long-chain SAM shows a less disordered situation leading to charge transfer through pinholes (light brown arrow) at the native Au surface, whereas the gold-thiol site involves charge transport within the monolayer (dark brown arrow).

solid–liquid (electrode–electrolyte) interfacial properties such as adhesion [12] and wettability [13,14]. Whitesides et al. [15,16] clarified the adsorption of alkanethiols with different chain lengths and concluded that long-chain alkanethiols are preferably adsorbed relative to short-chain derivatives of alkanethiols. The preferential adsorption of long-chain thiol molecules has been attributed to the higher cohesive interactions among long alkyl species in the monolayer, as reflected by the solubility difference between long-chain and short-chain adsorbates [17].

Traditionally, in the absence of redox-active species in the electrolyte or at the terminal head group, thiol-based SAMs on gold electrodes can be considered dielectric capacitors [18]. It has been observed that the SAM covers most of the electroactive sites [19] present on the Au surface and thus can restrict unwanted Au-electrocatalytic reactions under low-voltage operation [20]. However, potential-dependent faradaic currents for gold-monolayer-electrolyte systems exist even in the absence of redox-active moieties at pinholes or defect sites through ions [21] and electron tunneling at "collapsed" sites in the monolayer [22].

Fig. 1 depicts the gold-thiol SAM-electrolyte system consisting of the gold-SAM and the SAM–electrolyte interface as described by Gupta et al. [21]. Ideally, the functionalized alkane-thiol derivatives are expected to form a uniform, well-ordered array on the Au surface [23], as shown in Fig. 1(a). The packing density for closely packed thiol molecules on Au surface results in pinholes with radii almost similar to the atomic size of Au atoms [24]. The chemisorption of long-chain thiol molecules (C_6 and C_8) is much more ordered on gold than the smaller ones (C_3), which have been explained elsewhere [25,26]. Factors like inhomogeneities and surface roughness of the substrate affect the attachment of thiol molecules to the Au substrate, and thus, chances for an increased bare Au area persist [26].

It has been proposed that two main mechanisms are responsible for the leakage through SAM-covered Au-electrodes during electrical measurements. These are (1) the charge carrier penetration through pinholes (shown as a light brown arrow in Fig. 1(c)); and (2) the transport of charge carriers across the alkane backbone [21] (represented by the dark brown arrow in Fig. 1(c)). The pinholes are considered large enough to permit the percolation of ions in the electrolyte and the free electronic charges generated by the ionization of neutral or charged species in the monolayer or the electrolyte. The electron transfer through the insulating alkane backbone occurs through multiple mechanisms, tunneling, charge excitation to the LUMO level of the alkane chain, or thermal hopping of the electronic charge within the localized potential wells associated with each carbon atom of the alkane chain [27–35]. Once arriving at the native Au surface atoms, the charges experience a potential energy barrier at the interface due to the difference in the chemical potential. However, at the site of an Au-S bond, the chemical potential is equal at the interface region because the electrons bonded with these atomic orbitals are delocalized within this carbon chain. Additionally, the Fermi energy of electrons at the Au-monolayer

interface is slightly lower than surface electrons because of the shared electrons with the sulfur moiety [36,37].

The present article clarifies the impact of thiol-based SAMs as passivating agents for Au gate electrodes in EG-OFETs. We prepared functionalized n-alkanethiol ($CH_3(CH_2)_nSH$) based SAM electrodes, where n = 2, 5, and 7 refers to propanethiol (P-SAM), hexanethiol (H-SAM), and octanethiol (O-SAM), respectively. The performance of these passivated gate electrodes was measured with respect to a bulk Au as a reference gate electrode. We performed transfer curve measurements at a constant drain voltage (V_D = -0.4 V) with a gate voltage sweep (V_G) from 0.1 V to −0.4 V. Furthermore, long-term stability measurements of all the functionalized gates were carried out through 80 h of constant cyclic voltammetry (CV) experiments. Elemental compositions of the functionalized electrodes were clarified using XPS measurements before and after the electrical measurements to confirm the presence of thiol molecules on the gold surface.

2. Materials and methods

2.1. Materials details

Poly(3-hexylthiophene-2,5-diyl), P3HT (Sigma-Aldrich, regioregularity > 99%), with an average molecular weight of 17.5 g/mol, was employed as the semiconductor without extra processing. Commercially available phosphate-buffered saline (PBS) capsules comprised of 0.01 M phosphate buffer, 0.0027 M potassium chloride, and 0.137 M sodium chloride were purchased from Sigma-Aldrich and solved in Milli-Q water (18.2 MΩ·cm at 25 °C) to make a buffer solution with pH 7.4 at 25 °C. N-alkanethiol derivatives ($CH_3(CH_2)_nSH$) with n = 2, 5, and 7 i.e. n-propanethiol (C_3H_7SH), n-hexanethiol ($C_6H_{13}SH$), and n-octanethiol ($C_8H_{17}SH$) (99% pure) were purchased from Sigma–Aldrich and used with no further purification. Water (HPLC-grade), and ethanol grade, puriss. p.a. assay, ≥ 99.8 % from Sigma-Aldrich, was used without further purification. Polyethylene naphthalate (PEN) films were purchased from Teonex.

2.2. Device fabrication

Interdigitated Cr (5 nm)/Au (50 nm) electrodes deposited onto Si/SiO$_2$ (300 nm) substrate were received from Technical Research Centre of Finland. The channel width and length were 80800 μm and 5 μm, so the obtained W/L ratio was 16160. The substrates were cleaned for 10 min via ultrasonication, each using isopropanol (IPA) followed with deionized water. After that, a freshly prepared solution of P3HT in dichlorobenzene (DCB) of 4 mg/mL concentration was spin-coated (2000 rpm for 40 s) followed by annealing at 90 °C for 1 h on a hot plate in the dark. A 3D printed well with an adjacent reservoir was fixed on the substrate using the polydimethylsiloxane (PDMS) elastomer that stores the HPLC water acting as the electrolyte. Finally, the device was

incubated in HPLC water (electrolyte) overnight prior to measurements. Figure S1 (Supplementary Information) represents the schematic of the EG-OFET device with its various components.

2.3. Electrode fabrication

Commercially available PEN films with an adhesive layer were used as substrates for the thermal evaporation of a 50 nm thick Au layer. After evaporation, these substrates were ultrasonicated in IPA for 10 min, followed by 2 min of UV ozone treatment. The UV oxidized PEN-Au substrates were taken into a nitrogen atmosphere and placed in one of three 10 mM solutions containing either propanethiol (P-SAM), hexanethiol (H-SAM), or octanethiol (O-SAM), all dissolved in ethanol, depending on the desired thiol-SAM. The PEN-Au substrates were then incubated in these solutions for 16 h to allow adsorption and self-assembly of the desired thiol molecules on the Au surface. Afterward, the substrates were cleaned using ethanol and stored in ethanol in the refrigerator to minimize the oxidation of the SAM layer during the processing to achieve the highest quality films [26].

2.4. Atomic force microscopy

Atomic force microscopy (AFM) images were recorded on a Bruker Dimension Icon AFM by using tapping mode with intermittent contacts (model: ScanAsyst in Air, resonant frequency: 1 kHz, and force constant: 0.72 N m^{-1}, samples/line: 512, cantilever dimensions: 650 nm (Tip), 115 μm (Length), and 25 μm (Width)).

2.5. Stabilization measurement

The electrical measurements were performed using a Keithley 4200A-SCS Parameter Analyzer with EG-OFET devices using HPLC-grade water as the electrolyte. The electrical stability response of the thiol-SAM gate electrodes was recorded using the protocol developed for the biosensing and long-term stability measurements described elsewhere [1,38]. Briefly, two different electrodes, named reference gate (bulk Au electrode) and functionalized gate (thermally deposited Au electrode on PEN substrate passivated with different SAMs), were kept in contact with the HPLC water as an electrolyte. For stabilizing the channel, the drain current (I_D) and the gate current (I_G) were measured as a function of V_G (ranging from 0.1 V to −0.4 V to 0.1 V in steps of −0.01 V) at a constant drain voltage of −0.4 V until the change in maximum drain current ($I_{D,max}$) varies less than 2 % per hour as shown in Figure S2 (Supplementary Information). Moreover, all the curves were measured in the forward and reverse modes to monitor the occurrence of hysteresis. After the EG-OFET channel reached quasi-steady-state current values [38], a transfer curve was recorded and stored as the reference current level (before functionalized gate measurements). Once the channel was stable, the thiol-based SAM gate was mounted, and new cyclic transfer characteristics were recorded for 128 cycles. This latter process was carried out to stabilize the EG-OFET to the functionalized gate electrode threshold voltage. To ensure that the channel remains stable using different functionalized gates, transfer characteristics were measured using the reference gate electrode before and after each set of measurements.

2.6. Cyclic voltammetry measurement method

The long-term behavior of the passivated Au electrodes and their impact on the leakage currents were carried out through cyclic voltammetry (CV) measurements using a potentiostat (GAMRY Instruments Reference 600). We use an Ag/AgCl double-junction reference electrode (inner solution 3 M KCl, outer solution 1 M KNO$_3$), platinum (Pt) wire counter electrode, and the thiol-SAM functionalized electrode as the working electrode. The electrodes were placed in 10 mM PBS buffer solution. Electrical stress was applied using a voltage sweep on the

Table 1
Summary of the average roughness and RMS roughness of different gate electrodes with passivating SAM layers. The imaged area in all cases is 0.2 μm × 0.2 μm.

Samples/ Roughness	Average Roughness (R_a)	RMS Roughness (R_q)
Bare Au	0.78 nm	0.98 nm
P-SAM	0.94 nm	1.25 nm
H-SAM	0.94 nm	1.26 nm
O-SAM	0.96 nm	1.20 nm

working electrode from 0.1 V to −0.4 V to 0.1 V with 40 s delay between each sweep, for a total of 80 h (4900 cycles), while the cyclic current–voltage (I-V) curves were simultaneously recorded.

2.7. XPS measurement method

X-ray photoelectron spectroscopy analyses for studying the elemental compositions of the thiol-SAM electrodes were carried out on a PHI Quantum 2000 XPS Microprobe spectrometer (Physical Electronics) using a monochromatic Al K(α) X-ray source, with the X-ray settings of 100 μm, 25 W, 15 kV. The survey scan was acquired using a constant pass energy of 187.5 eV, and the detailed scans were acquired using constant pass energy of 58.7 eV. The measurements were carried out for sample thiol-SAM electrodes before and after the electrical characterization measurement with an EG-OFET device. The measurements comprise of survey runs as well as the binding energy associated with gold, carbon, sulfur, and oxygen elements.

3. Results and discussion

### 3.1. Morphological studies

The surface morphologies of the three different thiol-SAM gate electrodes (P-SAM, H-SAM and O-SAM) and a bare PEN-Au electrode have been explored using AFM [10,35]. The average roughness (R_a) and the root mean square roughness (R_q) of these surfaces are summarized in Table 1 and provide information of the topographies of the functionalized electrodes. Although the roughness values are similar for each SAM surface, visual inspection of the AFM images (Fig. 2) reveal similarities between bare Au and P-SAM (Fig. 2 (a, b)), as well as between H-SAM and O-SAM (Fig. 2 (c, d)).

3.2. Stabilization measurements

In Fig. 3 we show the first 128 transfer and gate-leakage curves for the SAM-functionalized Au-electrodes. The transfer curves show increased drain current during the initial stabilization process for each thiol-SAM. From the transfer curves in Fig. 3(a, c, e), we conclude that during the first 25 cycles, the SAM layers must reorganize under external bias conditions that led to the increase in the leakage current along with the significant change in V_{th} and $I_{D,max}$ [22]. The transfer curves recorded using the bulk Au reference electrode before and after measurements show less than 5 % change in the magnitude of $I_{D,max}$, without hysteresis, see Figure S2 (Supplementary Information), which confirms the EG-OFET reaching quasi-steady state during the stabilization procedure. The transfer curves follow the drain current equation for a field-effect transistor in the saturated region:

$$I_D = \frac{W}{2L}\mu C_{tot}(V_G - V_{th})^2 \tag{1}$$

Where $W(L)$ is the width (length) of the channel, μ, the mobility of the charge carriers, C_{tot} total EG-OFET capacitance, and V_{th} is the threshold voltage. Focusing on one thiol-SAM gate over 128 cycles, we observe that the curves noticeably shift along the gate voltage axis during the forward bias transfer, while the curve shapes remain similar,
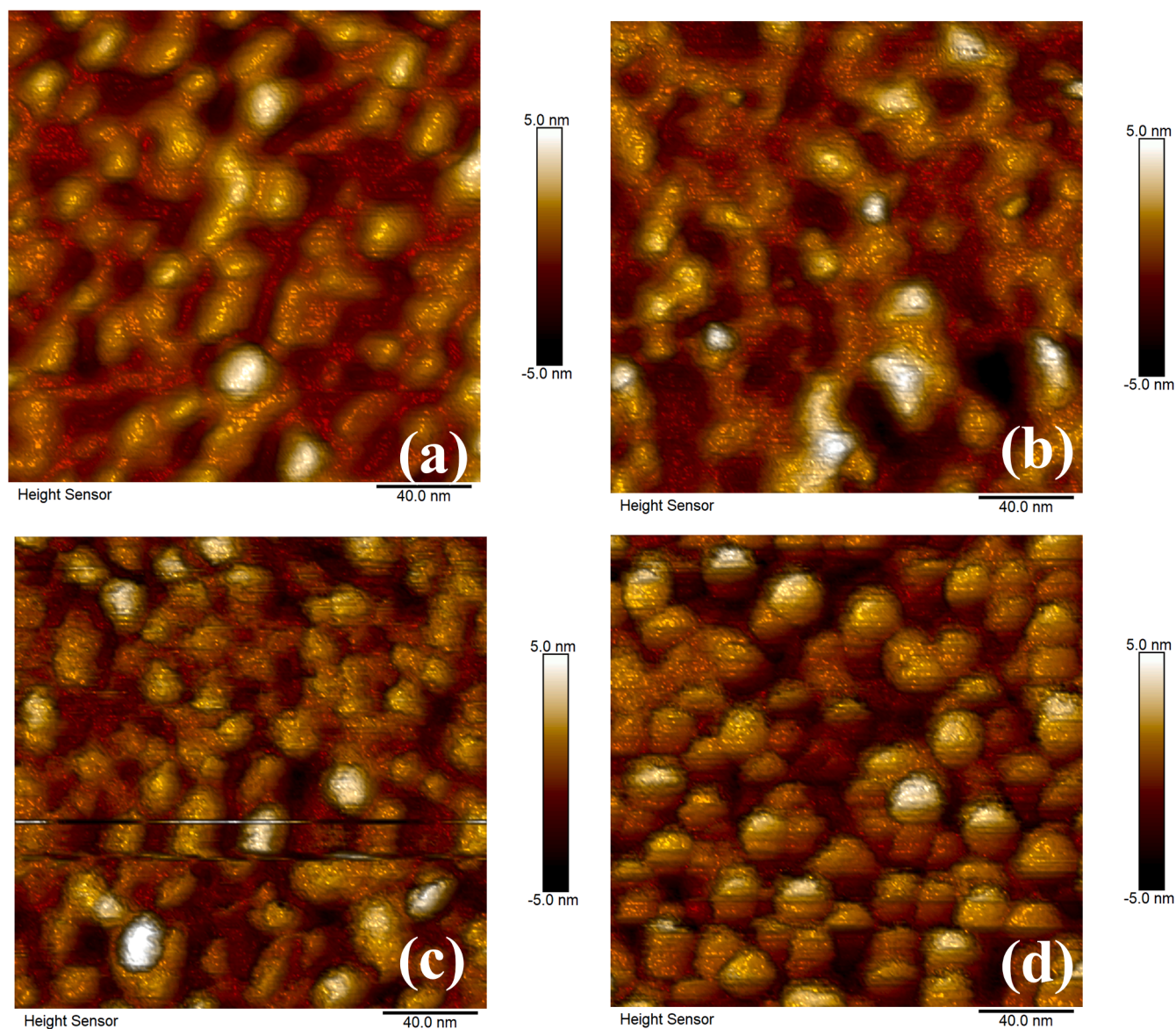
Fig. 2. Atomic forced microscopy images of four different gate electrodes namely (a) bare Au; (b) P-SAM; (c) H-SAM; and (d) O-SAM, respectively in 0.2 μm by 0.2 μm region.

see Figure S4 (Supplementary Information). Changes in C_{tot} will alter the shape of the curve, while changes in V_{th} will only shift the curve along the gate voltage axis. The reorganization of the SAM while cycling will therefore impact the work function of the electrode, shifting the V_{th}, while the total EG-OFET capacitance remain unchanged. As C_{tot} is the electrode/electrolyte and electrolyte/semiconductor interface capacitances in series, it is dominated by the smallest one. In this EG-OFET setup, the large double layer capacitance at the electrode/electrolyte interface implies that changes at that interface should not impact C_{tot} over the 128 transfer cycles [30]. Comparing instead the different thiol-SAM transfer curves to each other, Fig. 3(a, c, e), and to the bulk Au reference, Figure S4, we observe that the shapes are different, not just shifted, inferring that the difference in capacitance between the different SAMs is observable in this EG-OFET setup. By considering the electrode/electrolyte interface as another serially coupled capacitance consisting of a double layer capacitance (C_{DL}) and a blocking monolayer (C_{BL}), we can assume that C_{DL} is constant and C_{BL} is dependent on the chain length of the SAM (C_3, C_6 and C_8).

The compiled results of all measurements for the stabilization studies

($I_{D,max}$ vs cycle index) using the three different thiol-SAM electrodes can be seen in Fig. 4. We can see that the $I_{D,max}$ values vary over the measurements suggesting that the measured I_D depends on the device's history. However, the shape of the curves shows a similar response between sets of each thiol-SAM, allowing us to conclude that the response behaviors in each case were somewhat similar. To compare results between measurement sets, the $I_{D, max}$ values were normalized to the last value ($I_{D, max}$ at cycle 128), and the average normalized value and standard deviations for each cycle were calculated as shown in Fig. 4(b, d, f). In these Figures, we can observe the initial stabilization of the functional gate electrodes and the whole device. After about 50 transfer cycles, the standard deviation from the final 128th cycle is less than 5 % for each thiol-SAM electrode, suggesting that the EG-OFET has reached a new quasi-steady state which is dependent on the gate electrode. We can see that for P-SAM the $I_{D,max}$ value is always within 10% of its final, stabilized value. For H-SAM and O-SAM the initial $I_{D,max}$ values are almost 40% of the final value, but after approximately 25 cycles for both H-SAM and O-SAM, the values are within 10% of the final, stabilized $I_{D, max}$. This initial, drastic change for the longer chains can also be seen as a
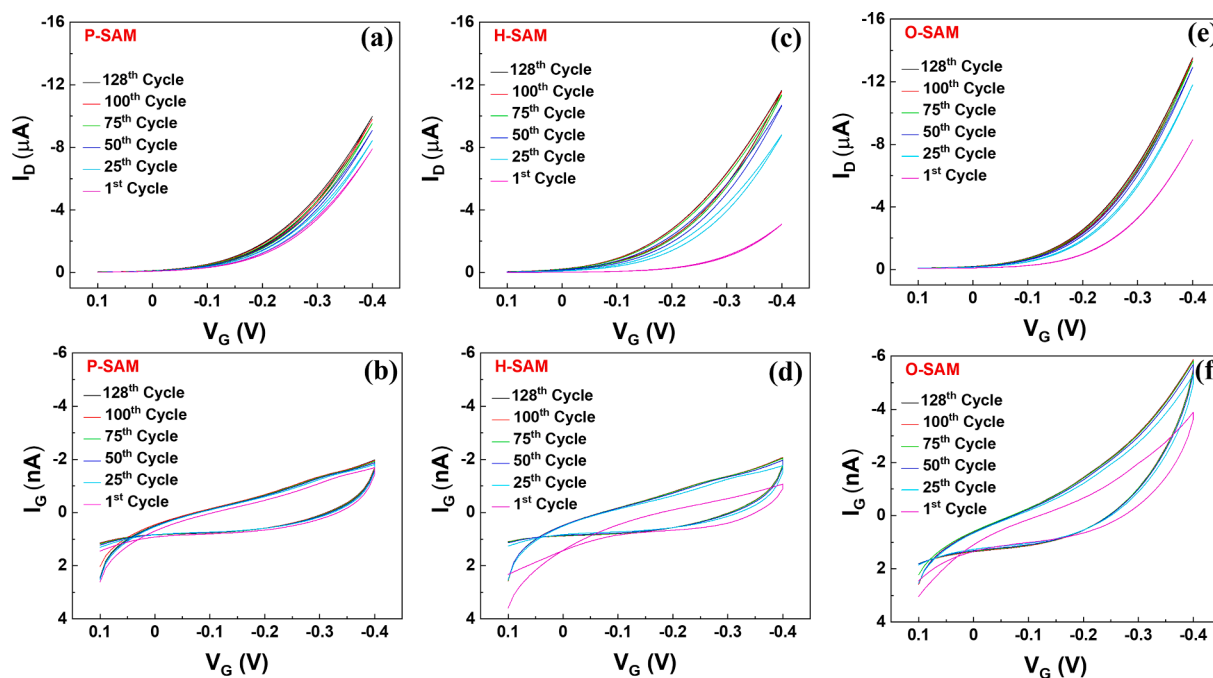
Fig. 3. Transfer and gate-leakage currents of the selected number of cycles (1st, 25th, 50th, 75th, 100th, and 128th) out of the total number of cycles (128 cycles) for each thiol-SAMs gate electrodes i.e. P-SAM (a, b), H-SAM (c, d), and O-SAM (e, f), respectively.
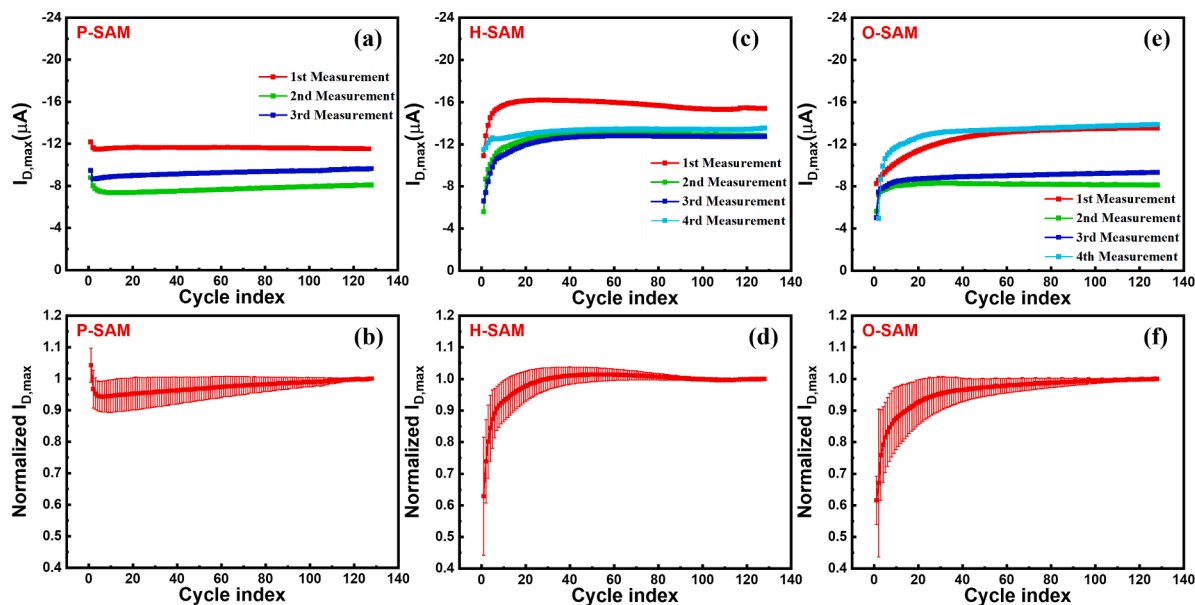

Fig. 4. Stabilization curves ($I_{D,max}$ vs Cycle index) of different measurement sets together with their average $I_{D,max}$ value, and standard deviation for each thiol-SAM, namely, P-SAM (a, b), H-SAM (c, d), and O-SAM (e, f).

shift in threshold voltage V_{th}, seen in Fig. 5, and can be attributed to the reorganization and change in surface potential under the external bias mentioned above.

Control experiments suggest that the device components, namely the organic semiconductor layer, dielectric, and gate electrode, remained largely unaffected during the electrical measurements because the device performance was almost similar before and after measurements, as observed via a reference bulk Au, Figure S3 (Supplementary Information). However, a consistent change in the transfer curves was observed. The threshold voltage shift and hysteresis were extracted from the transfer curves for all the thiol-based SAMs associated to individual measurement sets, as shown in Fig. 5(a, c). Furthermore, the normalized

curves (in Fig. 4(b, d)) that include the average value and standard deviation corresponding to each cycle were plotted as a function of the cycle index to compare these results for each thiol-based SAM. The threshold voltage was extracted using equation (1). The hysteresis value is calculated as the area between the forward and reversed biased sweeps in the transfer curves. It can be seen from Fig. 5(a, b) that, almost in all cases, the threshold voltage shifts towards more positive values during prolonged cycling and behaves similarly to the $I_{D,max}$ values, which is to be expected. However, forward-biased sweeps always show larger drain currents than backward ones. The cause for this hysteresis effect and its increase over the 128 cycles is most likely due to trapped charges inside the SAM, causing a minor shift in the V_{th}. However, as the
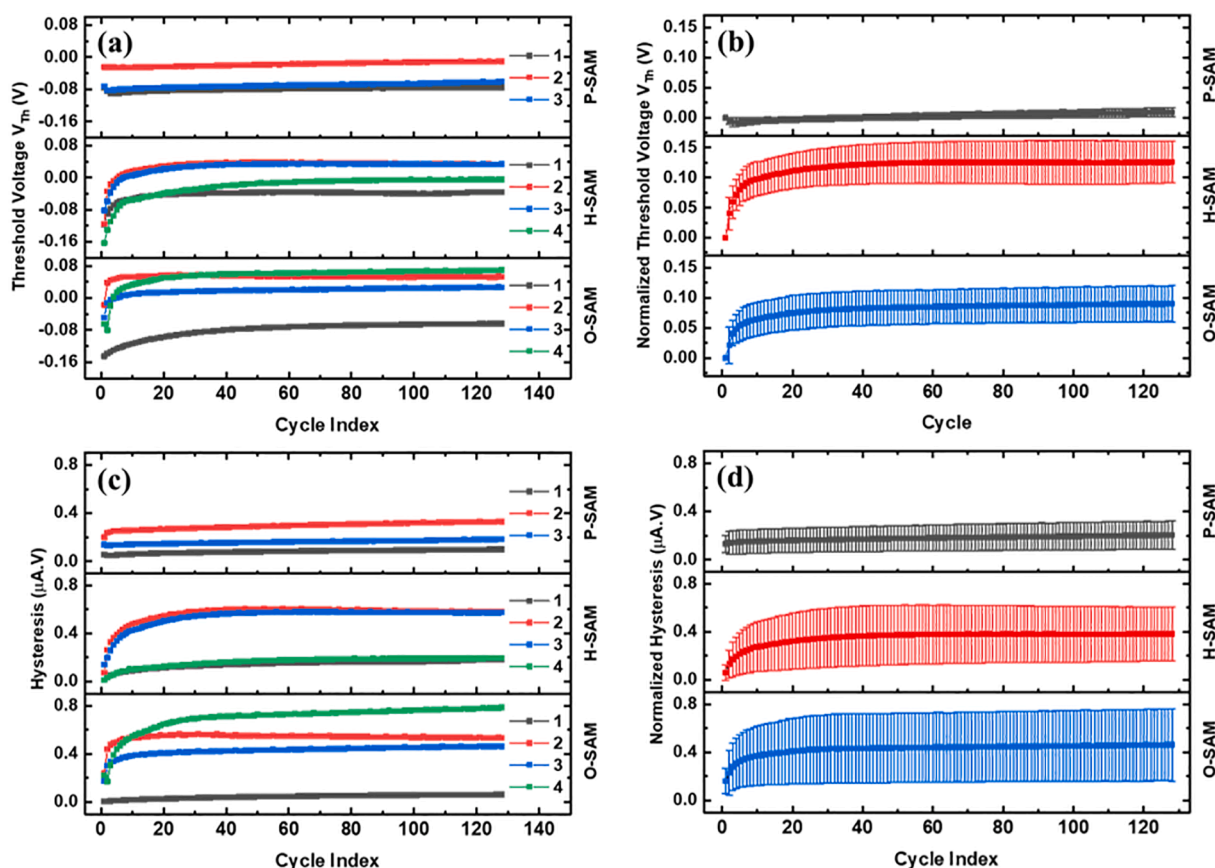
Fig. 5. Represents the threshold voltage shift (a, b) and hysteresis (c, d) together with their normalized curves for all cycles associated with different thiol-based sams as gate electrodes i.e., P-SAM, H-SAM, and O-SAM, respectively.

hysteresis varies between similar thiol-SAM electrodes, the exact mechanism can be very complex. As the pinhole mechanism dominates in the shorter P-SAM electrode, it will be the most similar to a bare Au electrode, see Figure S5 (Supplementary Information). Consequently, charge trapping in the P-SAM will be reduced compared to the longer H-SAM and O-SAM, resulting in less hysteresis, Fig. 5(c, d).

3.3. Cyclic voltammetry measurements

The long-term effects of the different SAM-functionalized electrodes have been clarified using CV measurements repeatedly for 80 h. The measured currents for the first and last cycle using the different working electrodes (bare Au, P-SAM, H-SAM, and O-SAM) can be seen in Fig. 6, while the evolution of the CV measurements can be seen in Figure S6 (Supplementary Information). The bare Au working electrode showed typical oxidation/reduction peaks reported in the literature [39] due to the absence of any passivating layer. In contrast, the current amplitude for all thiol-based SAM electrodes was initially small, suggesting that the thiol-SAMs passivate the Au electrode well. However, we observed that the response behavior associated with individual thiol-based working electrodes differs during 80 h of cyclic measurements. The inset in Fig. 6 (b) shows that the faradaic current decreases with increasing SAM length.
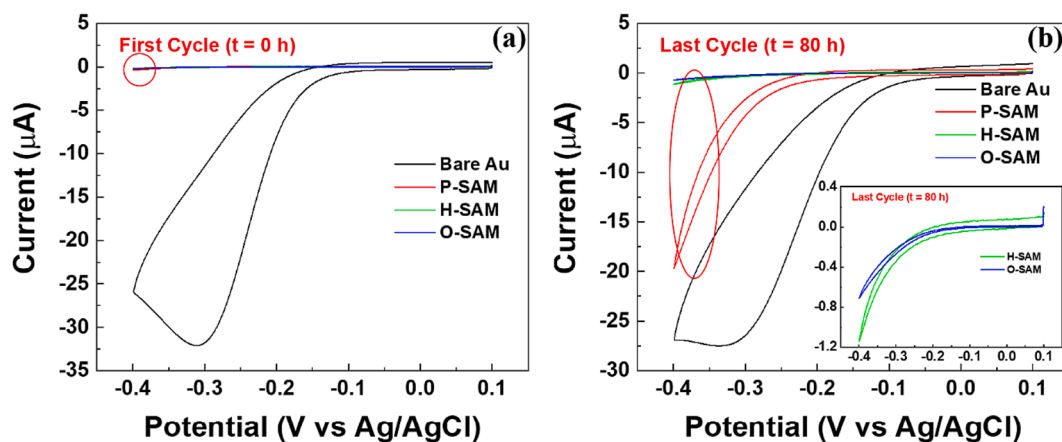
Fig. 6. Represent (a) the first cycle (t = 0 h), and (b) the last cycle (t = 80 h) of the CV curves corresponding to four different electrodes i.e., bare Au, P-SAM, H-SAM, and O-SAM, respectively.

Table 2

The average value and standard deviation of atomic composition (%) of C1s, O1s, S2p, Au4f and the elemental ratios of S w.r.t Au4f and C1s, before, and after electrical measurements.

At. % (Before)	C1s	O1s	S2p	Au4f	S/Au	S/C
P-SAM	20.10 ± 3.82	0.60 ± 0.85	0.36 ± 0.50	78.95 ± 4.17	0.01 ± 0	0.02 ± 0.03
H-SAM	20.15 ± 2.19	0.45 ± 0.35	1.30 ± 1.00	78.2 ± 3.54	0.02 ± 0.02	0.06 ± 0.06
O-SAM	25.50 ± 2.40	0 ± 0	2.60 ± 0.14	71.90 ± 2.55	0.04 ± 0.01	0.10 ± 0
At. % (After)	C1s	O1s	S2p	Au4f	S/Au	S/C
P-SAM	26.70 ± 7.35	6.75 ± 0.21	1.35 ± 0.49	65.20 ± 7.64	0.02 ± 0.01	0.05 ± 0
H-SAM	32.26 ± 2.62	5.25 ± 0.78	1.90 ± 0	60.85 ± 3.04	0.03 ± 0	0.06 ± 0
O-SAM	31.85 ± 9.69	0.21 ± 0.28	2.45 ± 0.50	65.55 ± 10.53	0.04 ± 0.01	0.08 ± 0.01

This may come as a surprise, but it can be well understood based on the model proposed for these SAM layers. Since the propanethiol molecules are not long enough to organize properly on the thermally deposited Au surface [40], there is a higher possibility of pinholes formation in the case of P-SAM, leading to a considerable amount of faradaic currents. The smaller leakage currents in the case of the other two SAM molecules confirm that the pinhole density is considerably less due to the uniform chemisorption of long-chain thiol molecules over the active area of the Au surface. Thus, the charge permeation to the surface of these working electrodes occurs in a controlled fashion. It is quite difficult to make a quantitative fractional assessment of the surfaces composed of pinholes out of the total electrode active surface [41]. However, the quantitative analysis of SAM surface coverage can be evaluated as the ratio of the peak oxidation current for electrolyte (PBS buffer) at the SAM-modified electrode (I_{SAM}) to that measured at a bare Au surface (I_{Au}) [42–44]. The entity (I_{SAM}/I_{Ag}) × 100% is defined as the normalized percent of electrochemically active surface area (%EAS). It is assumed that the bare Au surface is 100% electrochemically active. The calculated values of %EAS for different SAM in PBS buffer medium after 80 h cyclic measurements are 71.4 %; 4.3 %; and 2.5 % respectively. This also confirms that the desorption in H-SAM and O-SAM functionalized electrodes is quite small as compared to P-SAM.

3.4. XPS studies of different thiol-based SAM electrodes

Elemental studies were carried out through XPS measurements to clarify the adsorption/desorption of different thiol molecules over the Au surface before and after the electrical measurements. The normalized peak intensity associated with gold in each sample (bare Au, P-SAM, H-SAM, and O-SAM) was used to avoid an unnecessary shift in the peak position during measurements, as shown in Figure S7(a, b) (Supplementary Information). However, the peak response in context to sulfur element in each sample is noisy but shows a peak around 162.3 eV that confirms the presence of sulfur [42,45], Figure S7(c, d), both before and after electrical measurements.

Table 2 summarizes the atomic composition (%) of these elements (C1s, O1s, S2p, and Au4f) associated with each thiol-based SAM electrode before and after the electrical measurements. We observed increased carbon contents (before and after measurements) with increasing alkyl chain length. However, the carbon concentration also increased in each electrode after the measurements. The opposite trend was observed for the Au content, indicating that some chemical reaction must occur between the electrolyte and SAM molecules adhered over the Au surface. The increase in the oxygen contents in each sample after measurement supports this claim. The deconvolution of the C1s peaks is shown in Fig. 7, which also suggests an extra component associated with
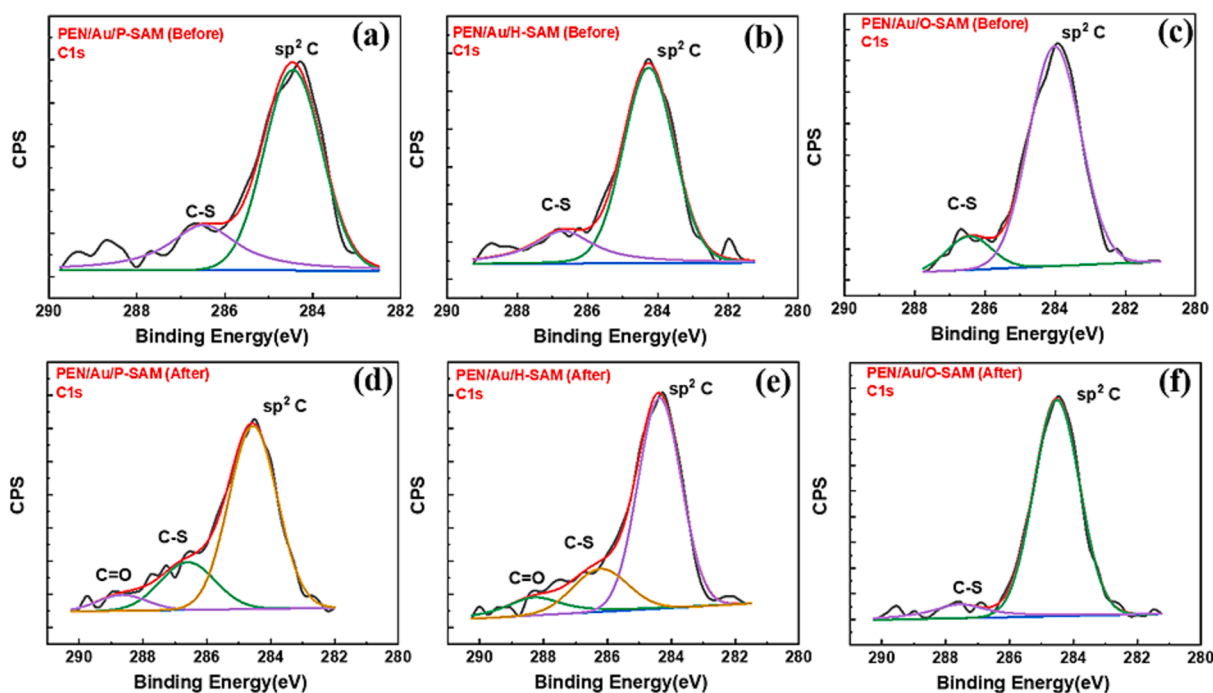

Fig. 7. Deconvolution of C1s peaks for each thiol-based SAM electrodes before and after measurements i.e. (a, d) P-SAM, (b, e) H-SAM, and (c, f) O-SAM.

the oxidation of carbon. However, this component was not prominent in the case of the O-SAM electrode. Finally, the elemental ratio of sulfur w. r.t. carbon and Au was found to be similar without much change (change within the error bar), which suggests the SAM layer was still present even after applying the electrical stress (128 cycles) to the thiol-based SAM electrodes. The deconvolution of C1s peaks in Fig. 7 was performed in each case to identify different chemical bonds. The peak position associated with different chemical bonds was within the error margin of $\pm 1\%$, as reported in the literature [46,47].

4. Conclusion

In conclusion, we have explored that the n-alkanethiol SAMs can be employed as a passivating layer on thermally deposited Au as gate electrodes for EG-OFETs. We have clarified the stabilization under the constant voltage-bias condition. We observed that these functionalized gates showed an initial increase in the maximum drain current, a positive threshold voltage shift, and increased hysteresis due to the contribution of ionic charges through pinholes. The shortest, P-SAM, has the most significant number of pinholes due to its disordered nature. When employed as a passivation layer on an Au electrode, it behaves similarly to bare Au, as evidenced by the transfer measurement cycling. Visual inspection of AFM images also suggests similarities between P-SAM and bare Au. The cyclic voltammetry measurements also show that it is unsuitable for long-term passivation. The longer H-SAM and O-SAM form more ordered layers and will act as better passivating agents. However, the changes in the device figures of merits, threshold voltage, and hysteresis for these SAMs are more significant, but they show better stability over time, as confirmed by long-term CV measurements. With XPS, we could confirm the presence of sulfur molecules before and after the measurements, meaning that the SAMs remain intact and adsorbed to the gold surface together with its oxidation after electrical measurements.

CRediT authorship contribution statement

Amit Tewari: Validation, Formal analysis, Visualization, Data curation, Investigation, Writing – original draft, Writing – review & editing. **Kim Björkström:** Validation, Formal analysis, Visualization, Investigation, Writing – review & editing. **Amir Mohammad Ghafari:** Data curation, Investigation, Visualization. **Eleonora Macchia:** Formal analysis, Resources. **Luisa Torsi:** Conceptualization, Supervision, Methodology, Writing – original draft. **Ronald Österbacka:** Conceptualization, Supervision, Project administration, Methodology, Writing – original draft.

Declaration of Competing Interest

The authors declare that they have no known competing financial interests or personal relationships that could have appeared to influence the work reported in this paper.

Data availability

Data will be made available on request.

Acknowledgements

Appendix A. Supplementary data

Supplementary data to this article can be found online at https://doi.org/10.1016/j.flatc.2023.100553.

References

[1] E. Macchia, L. Sarcina, C. Driescher, Z. Gounani, A. Tewari, R. Osterbacka, G. Palazzo, A. Tricase, Z.M. Kovacs Vajna, F. Viola, F. Modena, M. Caironi, F. Torricelli, I. Esposito, L. Torsi, Single-Molecule Bioelectronic Label-Free Assay of both Protein and Genomic Markers of Pancreatic Mucinous Cysts' in Whole Blood Serum, Advanced Electronic Materials 7 (2021), https://doi.org/10.1002/aelm.202100304.

[2] E. Macchia, K. Manoli, B. Holzer, C. Di Franco, M. Ghittorelli, F. Torricelli, D. Alberga, G.F. Mangiatordi, G. Palazzo, G. Scamarcio, L. Torsi, Single-molecule detection with a millimetre-sized transistor, Nature Communications 9 (2018), https://doi.org/10.1038/s41467-018-05235-z.

[3] D. Blasi, F. Viola, F. Modena, A. Luukkonen, E. MacChia, R.A. Picca, Z. Gounani, A. Tewari, R. Österbacka, M. Caironi, Z.M. Kovacs Vajna, G. Scamarcio, F. Torricelli, L. Torsi, Printed, cost-effective and stable poly(3-hexylthiophene) electrolyte-gated field-effect transistors, J Mater Chem C Mater. 8 (2020) 15312–15323, https://doi.org/10.1039/d0tc03342a.

[4] A.W. Adamson, A.P. Gast, Physical Chemistry of Surfaces, 6th Editio, Wiley Interscience, New York (1997), https://doi.org/10.1524/zpch.1999.210.Part_1.134.

[5] K.L. Prime, G.M. Whitesides, Adsorption of Proteins onto Surfaces Containing End-Attached Oligo(ethylene oxide): A Model System Using Self-Assembled Monolayers, Journal of the American Chemical Society 115 (1993) 10714–10721, https://doi.org/10.1021/ja00076a032.

[6] K.L. Prime, G.M. Whitesides, Self-assembled organic monolayers: Model systems for studying adsorption of proteins at surfaces, Science 252 (1991) (1979) 1164–1167, https://doi.org/10.1126/science.252.5009.1164.

[7] F. Leonardi, A. Tamayo, S. Casalini, M. Mas-Torrent, Modification of the gate electrode by self-assembled monolayers in flexible electrolyte-gated organic field effect transistors: Work function, Vs. capacitance effects, RSC Adv. 8 (2018) 27509–27515, https://doi.org/10.1039/c8ra05300f.

[8] J. Chen, B. Chang, S. Oyola-Reynoso, Z. Wang, M. Thuo, Quantifying Gauche Defects and Phase Evolution in Self-Assembled Monolayers through Sessile Drops, ACS Omega 2 (2017) 2072–2084, https://doi.org/10.1021/acsomega.7b00355.

[9] S.Y. Kim, S.J. Cho, S.E. Byeon, X. He, H.J. Yoon, Self-Assembled Monolayers as Interface Engineering Nanomaterials in Perovskite Solar Cells, Advanced Energy Materials 10 (2020), https://doi.org/10.1002/aenm.202002606.

[10] C.S.S. Sangeeth, L. Jiang, C.A. Nijhuis, Bottom-electrode induced defects in self-assembled monolayer (SAM)-based tunnel junctions affect only the SAM resistance, not the contact resistance or SAM capacitance, RSC Advances 8 (2018) 19939–19949, https://doi.org/10.1039/c8ra01513a.

[11] B. Liu, A.J. Bard, M.V. Mirkin, S.E. Creager, Electron Transfer at Self-Assembled Monolayers Measured by Scanning Electrochemical Microscopy, Journal of the American Chemical Society 126 (2004) 1485–1492, https://doi.org/10.1021/ja038611p.

[12] A. Rajca, An Introduction To Ultrathin Organic Films: From Langmuirblodgett To Self-Assembly, By Abraham Ulman, Academic Press, London 1991, Xxiii, 442Pp., $65, ISBN 0-12-708230-1, Advanced Materials. 4 (1992) 309–309. 10.1002/adma.19920040424.

[13] C.D. Bain, G.M. Whitesides, A Study by Contact Angle of the Acid-Base Behavior of Monolayers Containing ω-Mercaptocarboxylic Acids Adsorbed on Gold: An Example of Reactive Spreading, Langmuir 5 (1989) 1370–1378, https://doi.org/10.1021/la00090a019.

[14] L.H. Dubois, B.R. Zegarski, R.G. Nuzzo, Fundamental studies of microscopic wetting on organic surfaces. 2. Interaction of secondary adsorbates with chemically textured organic monolayers, Journal of the American Chemical Society 112 (1990) 570–579, https://doi.org/10.1021/ja00158a013.

[15] J.P. Folkers, P.E. Laibinis, G.M. Whitesides, Self-assembled Monolayers of Alkanethiols on Gold: Comparisons of Monolayers Containing Mixtures of Short- and Long-Chain Constituents with CH3 and CH2OH Terminal Groups, Langmuir 8 (1992) 1330–1341, https://doi.org/10.1021/la00041a015.

[16] P.E. Laibinis, R.G. Nuzzo, G.M. Whitesides, Structure of monolayers formed by coadsorption of two n-alkanethiols of different chain lengths on gold and its relation to wetting, Journal of Physical Chemistry. 96 (1992) 5097–5105, https://doi.org/10.1021/j100191a065.

[17] C.D. Bain, G.M. Whitesides, Formation of monolayers by the coadsorption of thiols on gold: Variation in the length of the alkyl chain, Journal of the American Chemical Society 111 (1989) 7164–7175, https://doi.org/10.1021/ja00200a040.

[18] D.D. Agonafer, E. Chainani, M.E. Oruc, K.S. Lee, M.A. Shannon, Study of insulating properties of alkanethiol self-assembled monolayers formed under prolonged incubation using electrochemical impedance spectroscopy, J Nanotechnol Eng Med. 3 (2012) 1–8, https://doi.org/10.1115/1.4007698.

[19] O. Chailapakul, C. Xu, R.M. Crooks, L. Sun, Interactions between Organized, Surface-Confined Monolayers and Vapor-Phase Probe Molecules. 7. Comparison of

Self-Assembling n-Alkanethiol Monolayers Deposited on Gold from Liquid and Vapor Phases, Journal of the American Chemical Society 115 (1993) 12459–12467, https://doi.org/10.1021/ja00079a029.

[20] M.I. Muglali, A. Bashir, M. Rohwerder, A study on oxygen reduction inhibition at pyridine-terminated self assembled monolayer modified Au(111) electrodes, Physica Status Solidi (A) Applications and Materials Science. 207 (2010) 793–800. 10.1002/pssa.200983321.

[21] C. Gupta, M.A. Shannon, P.J.A. Kenis, Electronic properties of a monolayer-electrolyte interface obtained from mechanistic impedance analysis, Journal of Physical Chemistry C. 113 (2009) 9375–9391, https://doi.org/10.1021/jp900918u.

[22] H.O. Finklea, S. Avery, M. Lynch, T. Furtsch, Blocking Oriented Monolayers of Alkyl Mercaptans on Gold Electrodes, Langmuir 3 (1987) 409–413, https://doi.org/10.1021/la00075a024.

[23] A. Ulman, An Introduction to Ultrathin Organic Thin Films From Langmuir-Blodgett to Self Assembly, Academic Press, San Diego, 1991.

[24] L.H. Dubois, R.G. Nuzzo, Synthesis, structure, and properties of model organic surfaces, Annual Review of Physical Chemistry 43 (1992) 437–463, https://doi.org/10.1146/annurev.pc.43.100192.002253.

[25] L.H. Dubois, B.R. Zegarski, R.G. Nuzzo, Molecular ordering of organosulfur compounds on Au(111) and Au(100): Adsorption from solution and in ultrahigh vacuum, The Journal of Chemical Physics 98 (1993) 678–688, https://doi.org/10.1063/1.464613.

[26] J.C. Love, L.A. Estroff, J.K. Kriebel, R.G. Nuzzo, G.M. Whitesides, Self-Assembled Monolayers of Thiolates on Metals as a Form of Nanotechnology, Self-assembled monolayers of thiolates on metals as a form of nanotechnology 36 (32) (2005), https://doi.org/10.1021/cr0300789.

[27] K. Slowinski, R.V. Chamberlain, C.J. Miller, M. Majda, Through-bond and chain-to-chain coupling, Two pathways in electron tunneling through liquid alkanethiol monolayers on mercury electrodes, J Am Chem Soc. 119 (1997) 11910–11919, https://doi.org/10.1021/ja971921l.

[28] K.N. Sze, S. M.; Kwok, Physics of Semiconductor Devices, Wiley Interscience, New York, United States, 2006.

[29] R.M. Hill Chelsea, Poole-frenkel conduction in amorphous solids, Philosophical Magazine. 23 (1971) 59–86, https://doi.org/10.1080/14786437108216365.

[30] G.D. Kong, S.E. Byeon, S. Park, H. Song, S.Y. Kim, H.J. Yoon, Mixed Molecular Electronics: Tunneling Behaviors and Applications of Mixed Self-Assembled Monolayers, Advanced Electronic Materials 6 (2020), https://doi.org/10.1002/aelm.201901157.

[31] G.D. Kong, H. Song, S. Yoon, H. Kang, R. Chang, H.J. Yoon, Interstitially Mixed Self-Assembled Monolayers Enhance Electrical Stability of Molecular Junctions, Nano Letters 21 (2021) 3162–3169, https://doi.org/10.1021/acs.nanolett.1c00406.

[32] L. Belding, S.E. Root, Y. Li, J. Park, M. Baghbanzadeh, E. Rojas, P.F. Pieters, H.J. Yoon, G.M. Whitesides, Conformation, and Charge Tunneling through Molecules in SAMs, Journal of the American Chemical Society 143 (2021) 3481–3493, https://doi.org/10.1021/jacs.0c12571.

[33] G.D. Kong, H. Song, H. Kang, J. Jin, S. Ayachi, H.J. Yoon, Reversing Molecular Dilution Effect by Varying the Bottom Electrode, Advanced Electronic Materials 8 (2022), https://doi.org/10.1002/aelm.202200645.

[34] E.A. Weiss, R.C. Chiechi, G.K. Kaufman, J.K. Kriebel, Z. Li, M. Duati, M.A. Rampi, G.M. Whitesides, Influence of defects on the electrical characteristics of mercury-drop junctions: Self-assembled monolayers of n-alkanethiolates on rough and smooth silver, Journal of the American Chemical Society 129 (2007) 4336–4349, https://doi.org/10.1021/ja0677261.

[35] F.C. Simeone, H.J. Yoon, M.M. Thuo, J.R. Barber, B. Smith, G.M. Whitesides, Defining the value of injection current and effective electrical contact area for egain-based molecular tunneling junctions, Journal of the American Chemical Society 135 (2013) 18131–18144, https://doi.org/10.1021/ja408652h.

[36] Q. Sun, A. Selloni, Interface and molecular electronic structure vs tunneling characteristics of CH 3- and CF 3-terminated thiol monolayers on Au(111), Journal of Physical Chemistry A. 110 (2006) 11396–11400, https://doi.org/10.1021/jp064905w.

[37] Charles Kittel, Herbert Kroemer - Thermal physics-W. H. Freeman, (1980) 496.

[38] A. Luukkonen, A. Tewari, K. Björkström, A.M. Ghafari, E. Macchia, F. Torricelli, L. Torsi, R. Österbacka, Long-term electrical characteristics of a poly-3-hexylthiophene water-gated thin-film transistor, Org Electron. (2023) 106844. 10.1016/j.orgel.2023.106844.

[39] Y. Zheng, Z. Huang, C. Zhao, S. Weng, W. Zheng, X. Lin, A gold electrode with a flower-like gold nanostructure for simultaneous determination of dopamine and ascorbic acid, Microchimica Acta. 180 (2013) 537–544, https://doi.org/10.1007/s00604-013-0964-0.

[40] J. Chen, Z. Wang, S. Oyola-Reynoso, M.M. Thuo, Properties of Self-Assembled Monolayers Revealed via Inverse Tensiometry, Langmuir 33 (2017) 13451–13467, https://doi.org/10.1021/acs.langmuir.7b01937.

[41] H.O. Finklea, Electrochemistry of Organized Monolayers of Thiols and Related Molecules on Electrodes, New York, 1996.

[42] M.H. Schoenfisch, J.E. Pemberton, Air stability of alkanethiol self-assembled monolayers on silver and gold surfaces, Journal of the American Chemical Society 120 (1998) 4502–5413, https://doi.org/10.1021/ja974301t.

[43] H. Khalid, E.M. Opodi, X. Song, Z. Wang, B. Li, L. Tian, X. Yu, W. Hu, Modulated Structure and Rectification Properties of a Molecular Junction by a Mixed Self-Assembled Monolayer, Langmuir (2022), https://doi.org/10.1021/acs.langmuir.2c01751.

[44] G.D. Kong, M. Kim, S.J. Cho, H.J. Yoon, Gradients of Rectification: Tuning Molecular Electronic Devices by the Controlled Use of Different-Sized Diluents in Heterogeneous Self-Assembled Monolayers, Angewandte Chemie. 128 (2016) 10463–10467, https://doi.org/10.1002/ange.201604748.

[45] R.G. Laibinis, P.E. Whitesides, G.M. Allara, D.L. Tao, Y-T. Parikh, A.N. Nuzzo, Comparison of the Structures and Wetting Properties of Self-Assembled Monolayers of n-Alkanethiols on the Coinage Metal Surfaces, Cu, Ag, Au, Journal of American Chemistry, Society 113 (1991) 7152–7167.

[46] H. Takiguchi, K. Sato, T. Ishida, K. Abe, K. Yase, K. Tamada, Delicate surface reaction of dialkyl sulfide self-assembled monolayers on Au(111), Langmuir 16 (2000) 1703–1710, https://doi.org/10.1021/la981450w.

[47] C. Jung, O. Dannenberger, Y. Xu, M. Buck, M. Grunze, Self-assembled monolayers from organosulfur compounds: A comparison between sulfides, disulfides, and thiols, Langmuir 14 (1998) 1103–1107, https://doi.org/10.1021/la9708851.